

# Identifying the Origin of Thermal Modulation of Exchange Bias in MnPS<sub>3</sub>/Fe<sub>3</sub>GeTe<sub>2</sub> van der Waals Heterostructures

Aravind Puthirath Balan,\* Aditya Kumar, Patrick Reiser, Joseph Vimal Vas, Thibaud Denneulin, Khoa Dang Lee, Tom G. Saunderson, Märta Tschudin, Clement Pellet-Mary, Debarghya Dutta, Carolin Schrader, Tanja Scholz, Jaco Geuchies, Shuai Fu, Hai Wang, Alberta Bonanni, Bettina V. Lotsch, Ulrich Nowak, Gerhard Jakob, Jacob Gayles, Andras Kovacs, Rafal E. Dunin-Borkowski, Patrick Maletinsky,\* and Mathias Kläui\*

The exchange bias phenomenon, inherent in exchange-coupled ferromagnetic and antiferromagnetic systems, has intrigued researchers for decades. Van der Waals materials, with their layered structures, offer an ideal platform for exploring exchange bias. However, effectively manipulating exchange bias in van der Waals heterostructures remains challenging. This study investigates the origin of exchange bias in MnPS<sub>3</sub>/Fe<sub>3</sub>GeTe<sub>2</sub> van der Waals heterostructures, demonstrating a method to modulate nearly 1000% variation in magnitude through simple thermal cycling. Despite the compensated interfacial spin configuration of MnPS<sub>3</sub>, a substantial 170 mT exchange bias is observed at 5 K, one of the largest observed in van der Waals heterostructures. This significant exchange bias is linked to anomalous weak ferromagnetic ordering in MnPS<sub>3</sub> below 40 K. The tunability of exchange bias during thermal cycling is attributed to the amorphization and changes in the van der Waals gap during field cooling. The findings highlight a robust and adjustable exchange bias in van der Waals heterostructures, presenting a straightforward method to enhance other interface-related spintronic phenomena for practical applications. Detailed interface analysis reveals atom migration between layers, forming amorphous regions on either side of the van der Waals gap, emphasizing the importance of precise interface characterization in these heterostructures.

## 1. Introduction

Exchange bias (EB) is a unidirectional anisotropy that occurs in exchange-coupled antiferromagnetic/ferromagnetic (AFM/FM) systems, such as thin films and core-shell nanostructures.<sup>[1–3]</sup> While this phenomenon has been studied in thin-film heterostructures for over four decades, a comprehensive theoretical understanding remains a challenge for the condensed matter physics community. It is now well established, that there is not just one specific origin of the exchange bias phenomenon. Instead, several theoretical models of EB in magnetic systems have been developed, considering various possible spin configurations at the interface, including in-plane (IP), collinear, perpendicular, and out-of-plane (OOP) arrangements.<sup>[3]</sup> Furthermore, EB has been extensively studied in polycrystalline AFM/FM interfaces, with the phenomenological aspects extensively discussed by O'Grady et al.<sup>[4]</sup> However, most theoretical models that effectively describe EB assume

A. Puthirath Balan, A. Kumar, T. G. Saunderson, G. Jakob, M. Kläui  
 Institute of Physics  
 Johannes Gutenberg University Mainz  
 Staudinger Weg 7, 55128 Mainz, Germany  
 E-mail: [aravindputhirath@uni-mainz.de](mailto:aravindputhirath@uni-mainz.de); [klaui@uni-mainz.de](mailto:klaui@uni-mainz.de)

P. Reiser, M. Tschudin, C. Pellet-Mary, D. Dutta, C. Schrader, P. Maletinsky  
 Department of Physics  
 University of Basel  
 Klingelbergstrasse 82, Basel CH-4056, Switzerland  
 E-mail: [patrick.maletinsky@unibas.ch](mailto:patrick.maletinsky@unibas.ch)

J. Vimal Vas, T. Denneulin, A. Kovacs, R. E. Dunin-Borkowski  
 Ernst Ruska-Centre for Microscopy and Spectroscopy with Electrons and  
 Peter Grünberg Institute  
 Forschungszentrum Jülich  
 52425 Jülich, Germany  
 K. D. Lee, J. Gayles  
 Department of Physics  
 University of South Florida  
 Tampa, FL 33620, USA

 The ORCID identification number(s) for the author(s) of this article can be found under <https://doi.org/10.1002/adma.202403685>

© 2024 The Author(s). Advanced Materials published by Wiley-VCH GmbH. This is an open access article under the terms of the [Creative Commons Attribution-NonCommercial-NoDerivs](https://creativecommons.org/licenses/by/4.0/) License, which permits use and distribution in any medium, provided the original work is properly cited, the use is non-commercial and no modifications or adaptations are made.

DOI: 10.1002/adma.202403685

well-defined AFM/FM interfaces devoid of roughness or grain boundaries.<sup>[2,5–7]</sup> In reality, thin-film heterostructures are susceptible to imperfect interfaces.<sup>[8–10]</sup> The emergence of van der Waals (vdW) magnetic materials offers a potential solution, providing a broad range of FM and AFM vdW materials.<sup>[11]</sup> Their inherent layered structure and ability to form heterostructures present a convenient means to obtain atomically flat single-crystalline AFM/FM interfaces, renewing interest in the investigation of EB in vdW heterostructures.<sup>[12]</sup>

Although vdW AFM/FM heterostructures offer potentially ideal interfaces for EB studies by providing well-defined compensated or uncompensated spin ordering with distinct magnetic anisotropy, most studies to date have yielded complex results with no clear correlation to the existing understanding of the EB phenomenon in thin-film heterostructures.<sup>[12]</sup> This necessitates a detailed characterization of the interface structure to reveal whether the flat surfaces that many individual flakes exhibit are retained also in heterostructures where the resulting interface structure can govern the coupling mechanisms. Furthermore, a weaker exchange coupling in van der Waals heterostructures hinders their suitability for storage applications because of the presence of the vdW gap.<sup>[13]</sup> Recent efforts have focused on extrinsic control of exchange coupling by manipulating the AFM/FM interface registry, involving methods like applying pressure and laser irradiation.<sup>[14,15]</sup> Recent successful experiments have demonstrated significant EB in vdW heterostructures through coverage control and the application of gate voltage.<sup>[16,17]</sup> Additionally, the introduction of an oxide layer has shown promise, albeit challenges in controllability and repeatability.<sup>[18,19]</sup> Despite these advances, a straightforward and efficient strategy to precisely tune EB in vdW heterostructures remains elusive. Such a strategy is crucial for enabling diverse applications that require tailored EB strengths, such as magnetic recording and data storage.

Here, to understand the interplay between interface structure, magnetic order, and exchange bias, we extensively investigate MnPS<sub>3</sub>/Fe<sub>3</sub>GeTe<sub>2</sub> AFM/FM vdW heterostructures in a multimodal approach, combining magnetotransport anomalous

Hall effect, superconducting quantum interference device (SQUID) magnetometry, scanning nitrogen-vacancy center magnetometry (S-NVM), and scanning transmission electron microscopy (STEM). Despite featuring a fully compensated AFM/FM interface,<sup>[20–22]</sup> the vdW MnPS<sub>3</sub>/Fe<sub>3</sub>GeTe<sub>2</sub> system exhibits a remarkably high interfacial exchange-coupling strength. This gives rise to a significant EB, one of the most substantial observed in van der Waals AFM/FM interfaces so far. Notably, the strength of interfacial coupling can be modulated through thermal cycling. This thermal manipulation results in a decisive alteration in the magnitude of EB, exceeding 1000%. This thermal cycling can be implemented concurrently with the field-cooling procedure used to establish EB, thus eliminating the need for any additional steps. The unprecedented and significant alteration in EB magnitude through straightforward thermal cycling may set a platform for manipulating various other interface-related spintronic phenomena in vdW heterostructures. The subsequent section summarizes and discusses the extensive EB observed in the MnPS<sub>3</sub>/Fe<sub>3</sub>GeTe<sub>2</sub> system, elucidating its origin and the evolution induced by thermal cycling.

## 2. Results and Discussion

To fabricate the device, we transfer a MnPS<sub>3</sub>/Fe<sub>3</sub>GeTe<sub>2</sub> heterostructure onto prefabricated Au/Cr (25/5 nm) Hall contacts deposited on a Si/SiO<sub>2</sub> (300 nm) substrate. We employ a polydimethylsiloxane (PDMS)- and polymethylmethacrylate (PMMA)-assisted dry transfer method inside an inert-atmosphere-maintained glove box to transfer and stack flakes of Fe<sub>3</sub>GeTe<sub>2</sub> and MnPS<sub>3</sub> in the specified order. This results in the formation of a MnPS<sub>3</sub>/Fe<sub>3</sub>GeTe<sub>2</sub> vdW heterostructure with a clean interface (refer to **Figure 1c** inset). To minimize the risk of oxidation due to brief exposure of the heterostructure to air during wire bonding of the voltage and current pads for anomalous Hall measurements, we cap the obtained heterostructure with a hexagonal boron nitride (h-BN) flake. Additionally, unless otherwise stated, special care is taken to limit the air exposure time to below 30 min in all the devices measured during this investigation. For a detailed sample preparation procedure, please refer to the Experimental Section. The wire-bonded device is loaded into a high-field cryostat, and anomalous Hall effect measurements are conducted using magnetotransport techniques. For comparison, we additionally carry out anomalous Hall effect measurements on freshly exfoliated Fe<sub>3</sub>GeTe<sub>2</sub> flakes capped by h-BN, summarized in the Supporting Information (refer to **Figure S1** in the Supporting Information).

To induce EB, a freshly prepared device consisting of h-BN-capped MnPS<sub>3</sub>/Fe<sub>3</sub>GeTe<sub>2</sub> vdW heterostructure is subjected to a field-cooling process starting from 120 K (a temperature above the Neel temperature of MnPS<sub>3</sub>, which is 78 K) down to the desired temperature ( $T = 5$  K) with an OOP magnetic field of +8 and –8 T. After reaching the desired temperature, the magnetic field is ramped down to zero, and the anomalous Hall voltage ( $V_{xy}$ ) measured by sweeping the field in the OOP direction. The normalized anomalous Hall voltage ( $V_{xy}$ ) is used to plot the hysteresis (refer to **Figure 1a**). The EB field ( $H_{EB}$ ) is determined using the formula  $H_{EB} = \frac{(H_C^+ + H_C^-)}{2}$  where  $H_C^+$  and  $H_C^-$  represent the positive and negative switching fields. Surprisingly, a large

T. G. Saunderson  
Peter Grünberg Institut and Institute for Advanced Simulation  
Forschungszentrum Jülich and JARA  
52425 Jülich, Germany  
T. Scholz, B. V. Lotsch  
Max Planck Institute for Solid State Research  
Heisenbergstraße 1, 70569 Stuttgart, Germany  
J. Geuchies, S. Fu, H. Wang  
Max Planck Institute for Polymer Research Mainz  
Ackermannweg 10, 55128 Mainz, Germany  
A. Bonanni  
Institute of Semiconductor and Solid-State Physics  
Johannes Kepler University Linz  
Altenberger Straße 69, Linz 4040, Austria  
U. Nowak  
Department of Physics  
University of Konstanz  
Universitaetsstrasse 10, 78464 Konstanz, Germany  
M. Kläui  
Center for Quantum Spintronics  
Department of Physics  
Norwegian University of Science and Technology  
Trondheim 7491, Norway

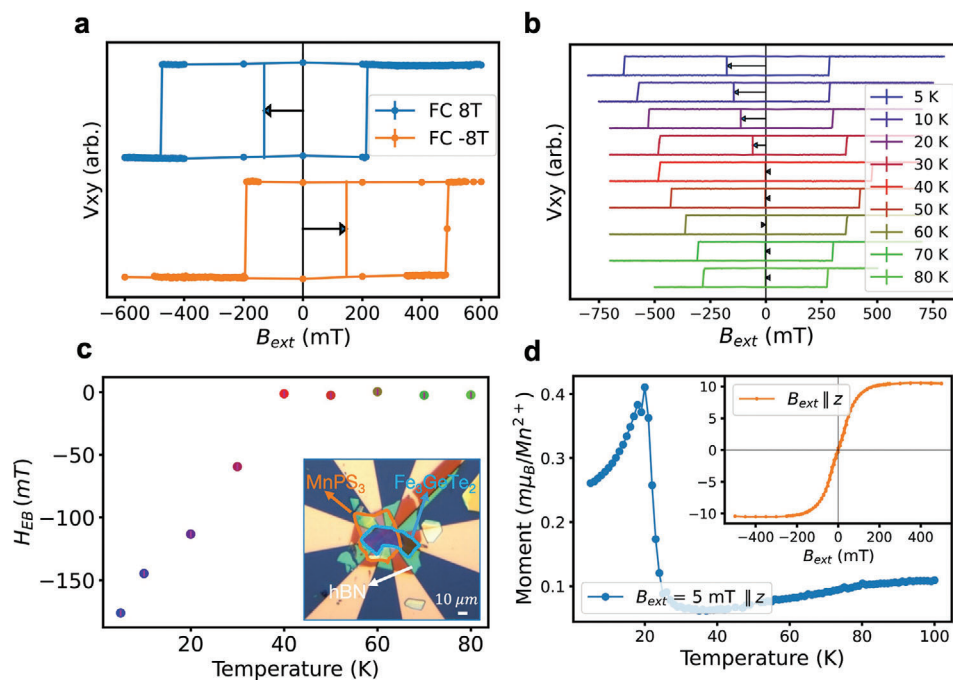


**Figure 1.** a) Anomalous Hall voltage ( $V_{xy}$ ) as a function of the magnetic field after  $\pm 8$  T field-cooling process measured at 5 K, b)  $V_{xy}$  as a function of the magnetic field after + 8 T field cooling and measured at temperatures ranging from 5 to 80 K. c) The  $H_{EB}$  versus  $T$  plot, derived from the data presented in (b), reveals the blocking temperature of  $\text{MnPS}_3$  to be  $\approx 40$  K. The inset provides an optical image of the measured van der Waals heterostructure. d) Magnetization ( $M$ ) versus temperature ( $T$ ) curve measured for the bulk  $\text{MnPS}_3$  crystal in an OOP orientation. The inset displays an isothermal  $M$  versus  $H$  curve at 5 K.

negative  $H_{EB}$  of magnitude 170 mT is observed at 5 K. We note that this large exchange bias is observed in a comparably thick (80 nm  $\text{Fe}_3\text{GeTe}_2$ ) layer and while the thickness dependence of exchange bias in vdW heterostructures can be complex as, for instance, shown and discussed in ref. [23], one can expect that by varying the thicknesses, the exchange bias can be further tuned. A complete thickness dependence study is however beyond the scope of this work. It is important to note that this large exchange bias observed is unexpected, considering the previously claimed fully compensated magnetic order of  $\text{MnPS}_3$ .<sup>[21,22,24–26]</sup> Continuing our investigation, we measure the trend of  $H_{EB}$  as a function of increasing temperature by executing a similar procedure at various temperatures, ranging from 5 to 80 K (refer to Figure 1b).  $H_{EB}$  is calculated for each measurement and plotted against the temperature, as illustrated in Figure 1c. It is evident that  $H_{EB}$  is at a maximum (170 mT) at 5 K and gradually decreases with increasing temperature, disappearing at 40 K—well below the Neel temperature ( $T_N$ ) of  $\text{MnPS}_3$  (78 K). The presence of such a large EB that disappears at a temperature much lower than the  $T_N$  cannot be solely explained by the compensated antiferromagnetic order of  $\text{MnPS}_3$ .

To understand more about the origin of EB, we employ DC SQUID magnetometry to obtain magnetization versus temperature ( $M$  vs  $T$ ) and magnetization versus magnetic field ( $M$  vs  $H$ ) plot at 5 K for a bulk  $\text{MnPS}_3$  crystal while maintaining the magnetic field orientation OOP. The results are depicted in Figure 1d. Below 40 K, an anomalous magnetic moment is observed, as indicated by the onset in the magnetic moment. The emergence of this anomalous ferromagnetic moment below 40 K is also ob-

served in the temperature dependence of spin Hall magnetoresistance in  $\text{MnPS}_3/\text{Pt}$  device (refer to Figure S2 in the Supporting Information). The onset of this anomalous moment correlates with the onset of the nonzero  $H_{EB}$  (refer to Figure 1c). A clear saturation in  $M$  versus  $H$  hysteresis at 5 K with finite coercivity is presented as further supporting evidence (see Figure 2d inset).

To investigate the nature and anisotropy of the anomalous ferromagnetic moment in  $\text{MnPS}_3$  flakes, we next utilize S-NVM. To probe the static magnetic state of a few-layer  $\text{MnPS}_3$  of comparable thickness to the  $\text{Fe}_3\text{GeTe}_2/\text{MnPS}_3$  heterostructure under investigation, S-NVM is performed on isolated  $\text{MnPS}_3$  flakes at 4.5 K. The nitrogen-vacancy (NV) center can be scanned across the sample to record the emanating stray magnetic field. This enables the inference of the underlying magnetization, with a typical spatial resolution of 30–100 nm (Figure 2a and details in the Experimental Section). The examined sample comprises two isolated  $\text{MnPS}_3$  flakes capped by a h-BN flake (see Figure 2a).

We find that a clear stray magnetic field arises from the edge of the  $\text{MnPS}_3$  flake, indicating an uncompensated magnetic moment that deviates from its expected compensated antiferromagnetic order (see Figure 2b). A linecut is taken across the flake edge with an applied field of 150 mT along the NV axis and a magnetic model of a homogeneous magnetization is fitted to the stray field. The best agreement between the model and the data is found for Mn magnetic moments pointing along the IP direction parallel to the NV center projection to the sample plane. A magnetization of  $M = 2170 (\pm 40) \mu_B \text{ nm}^{-2}$  is obtained corresponding to a bulk magnetization of  $15.8 (\pm 0.3) \mu_B$  per unit cell for the flake thickness of  $57.5 (\pm 4.5) \text{ nm}$  obtained by the simultaneously recorded

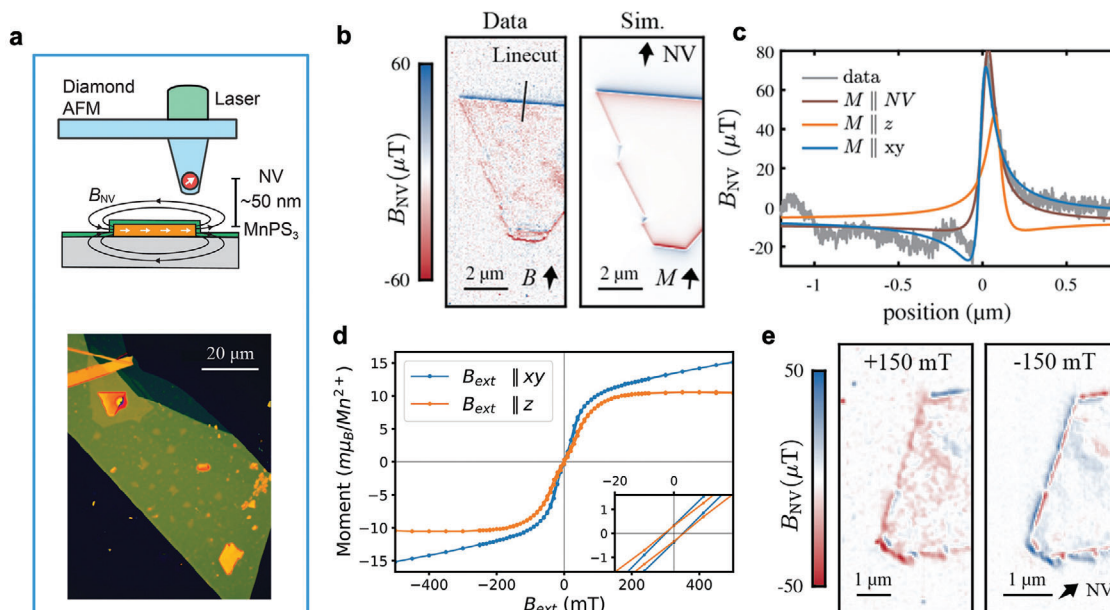


**Figure 2.** a) Schematics of S-NVM setup: a NV center is brought into contact with the surface, and the stray magnetic field of the sample is recorded by performing an optically detected magnetic resonance (ODMR) measurement at each pixel with the microscope image of the studied sample underneath. It comprises two MnPS<sub>3</sub> flakes of  $\approx 50$  nm height capped by h-BN. b) Stray magnetic field image of the flake recorded at  $B_{\text{ext}} = 150$  mT applied along the NV axis as indicated by the arrows. Simulation of the stray magnetic field assuming IP orientation of the magnetization. c) Linecut taken across the edge of the flake as indicated by the line. Different magnetization models are used to fit the data. The best agreement is found with the IP orientation of the flake. d) DC SQUID magnetometry data of a bulk crystal taken at 5 K. Though bulk MnPS<sub>3</sub> is reported to be an ideal Heisenberg AFM, a finite magnetic moment with remanence is observed, suggesting a transition in spin ordering at low temperatures. e) Stray magnetic field image for opposite field polarities. Reversing field polarity between +150 and  $-150$  mT yields opposite polarity of the stray field, indicating a switchable weak ferromagnetic ordering.

topography (refer to Figure 2c). Using these parameters, the stray field of the flake is simulated, and a good qualitative agreement between data and simulation indeed confirms the easy plane anisotropy of the Mn moments. This finding is in good agreement with the recent report that suggests MnPS<sub>3</sub> undergoes a spin-reorientation transition, characterized by Mn moments that go from an OOP Heisenberg-type collinear antiferromagnetic order to the IP XY-type order (refer to the schematic in Figure S2b in the Supporting Information).<sup>[27]</sup> Such a low-temperature spin-reorientation transition has also been independently observed by Han et al. in their recent experiments.<sup>[28]</sup> A larger magnetization (see Figure 2d) is observed for the magnetic hysteresis ( $M$  vs  $H$ ) measured with the sweeping field oriented IP with respect to the bulk MnPS<sub>3</sub> crystal as compared to that when the sweeping field is oriented OOP, which provides further supporting evidence for the IP anisotropy.

In agreement with the measurements on the bulk crystal, at lower fields, the uncompensated moment shows a linear field dependence of  $(\partial M / \partial B_{\text{ext}}) = 92 (\pm 9) \text{ m} \frac{\mu_B}{\text{Mn}} / T$  (refer to Figure S3 in the Supporting Information) with a finite remanent magnetic moment of  $1.5 (\pm 0.7) \text{ m} \mu_B / \text{Mn}$  close to zero field. Importantly, the remanent moment maintains the magnetization direction unchanged at lower fields even after reversing the polarity, as evident from identical red contrast observed in images acquired at  $\pm 5$  mT (refer to Figure S4 in the Supporting information). It is apparent from the S-NVM measurements that the remanent moment can potentially be bound to the AFM state of MnPS<sub>3</sub> and persists even above the maximum applied field of  $\mp 500$  mT (the

maximum field reachable by the used vector magnet) along the NV direction. However, the stray fields measured at  $\pm 150$  mT, as indicated in Figure 2e, exhibit an inverted contrast. This observation suggests that few-layer MnPS<sub>3</sub> flakes possess a larger switchable magnetic moment (below  $\pm 150$  mT). This magnetic moment displays a linear variation with the applied field and predominates over the discernible remanent moment bound to the AFM state of MnPS<sub>3</sub>, thereby contributing to the finite coercivity (refer to Figure S3 in the Supporting information).

Albeit of a soft magnetic nature, the field required to switch the uncompensated moment of the MnPS<sub>3</sub> flake is greater than 5 mT, whereas the bulk crystal has a coercive field of less than 5 mT (refer to Figure 2d inset). This contrasting behavior between bulk crystal and an exfoliated flake could be attributed to confinement effects.<sup>[20]</sup> Nevertheless, the few-layer MnPS<sub>3</sub> flake exhibits a remanent magnetic moment bound to the AFM state of MnPS<sub>3</sub>. This distinctive magnetic moment serves as a pinning source, thus possibly explaining the observed EB in the Fe<sub>3</sub>GeTe<sub>2</sub>/MnPS<sub>3</sub> heterostructures.

The findings from bulk SQUID magnetometry and high resolution (HR) and high sensitivity S-NVM measurements unequivocally establish the presence of net uncompensated magnetic moment in MnPS<sub>3</sub>. The observed EB can be ascribed to the pinning of Fe<sub>3</sub>GeTe<sub>2</sub> by the intrinsic weak anomalous magnetic moment associated with the AFM state in MnPS<sub>3</sub> flakes at temperatures below 40 K. This phenomenon arises due to a low-temperature spin-reorientation transition from OOP Heisenberg-type order to IP XY-type order.<sup>[27,28]</sup> The emergence

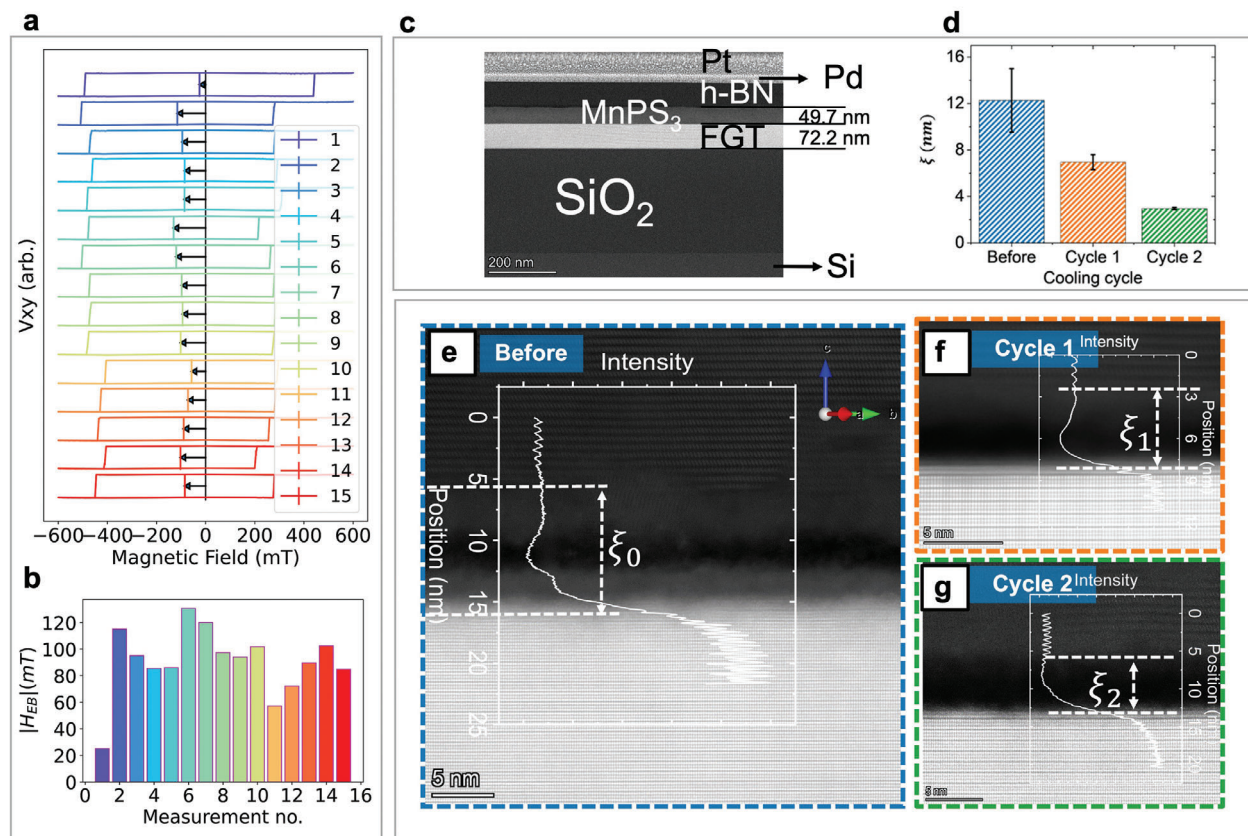


**Figure 3.** Evolution of EB due to change in van der Waals gap caused by heating-cooling cycles. a) AHE hysteresis loops measured after each field-cooling cycle consecutively for 15 times. b) The magnitude of EB varies between 25 and 132 mT. More measurements on additional samples can be found in the Supporting Information. c) Low magnification cross-sectional HAADF-STEM image of the Fe<sub>3</sub>GeTe<sub>2</sub>/MnPS<sub>3</sub>/h-BN vdW heterostructure. d) A bar graph summarizing the observed modification of intercrystalline distances ( $\xi$ ) measured in the images e–g) at room temperature before (e) and after two consecutive cooling and heating cycles (f and g), (e) a high-resolution HAADF-STEM image of the sample, and  $\xi_0$  is the intercrystalline distance measured at room temperature. The measurements were repeated 2 more times after cooling–heating cycles (f) and (g), and  $\xi_1$  and  $\xi_2$  are the corresponding intercrystalline distances measured. The intercrystalline distances measured after each cycle ( $\xi_1$  and  $\xi_2$ ) differed from the initial value ( $\xi_0$ ).

of a robust EB resulting from a low-temperature compensated AFM to weak FM transition has not been previously documented in vdW heterostructures. This observation has repercussions that could enable spintronic phenomena in MnPS<sub>3</sub> and other similar vdW systems, where such transitions can occur.

Having established the origin of EB, we next study the evolution of the  $H_{EB}$  strength. We find that the observed  $H_{EB}$  at a specific temperature undergoes a substantial variation, characterized by a dynamic evolution across successive iterations while maintaining experimental conditions unchanged. To systematically study this, we revisit device 1 (D1), a h-BN-capped MnPS<sub>3</sub>/Fe<sub>3</sub>GeTe<sub>2</sub>, and conduct 15 consecutive anomalous Hall voltage measurements at 5 K while implementing an 8 T field-cooling from 120 K, depicted in Figure 3a. We determine  $H_{EB}$  for each measurement and plot in a bar graph (refer to Figure 3b). Surprisingly, despite maintaining identical experimental conditions, we observe different values of  $H_{EB}$  after every heating and field-cooling cycle. To assess the universality of this observed metamorphosis, we fabricate two additional h-BN-capped MnPS<sub>3</sub>/Fe<sub>3</sub>GeTe<sub>2</sub> devices (device 2 and device 3) and follow a similar measurement protocol to obtain  $H_{EB}$  for 15 consecu-

tive field-cooling measurements. All three devices consistently demonstrate that a freestanding vdW AFM–FM interface is dynamic under thermal cycling, strongly influencing interface-related phenomena, particularly EB. The distribution of the evolving EB observed for 15 consecutive field-cooling measurements at 5 K for D1, D2, and D3 are summarized in Figure S5 (Supporting Information). However, the statistical distribution of EB among these three devices is not identical as evident from Figure S6 (Supporting Information) that refers to an indeterministic variation throughout 15 cycles. To understand this intriguing thermal evolution of EB quantitatively, we consider a simplistic expression for  $H_{EB}$  in an exchange-biased AFM/FM system, provided by the modified Meiklejohn–Bean model, as delineated in Equation (1) presented below:<sup>[29]</sup>

$$H_{EB} = \frac{J_{EB}}{\mu_0 M_{FM} t_{FM}} \quad (1)$$

where  $J_{EB}$  is the interfacial exchange-coupling energy,  $M_{FM}$  is the saturation magnetization of the FM, and  $t_{FM}$  is the thickness of the ferromagnetic layer. Now, the thermal-cycling-induced

evolution of EB can only be influenced by the parameter of the numerator  $J_{\text{EB}}$  while the denominator remains unchanged since the materials remain unaltered. Nevertheless, the numerator  $J_{\text{EB}}$ , directly linked to the interface characteristics, may be contingent upon the intercrystalline distance ( $\xi$ ) – the separation between respective crystalline regions of AFM and FM separated by a vdW gap. Recently, Huang et al. conducted measurements of EB in FM/AFM vdW heterostructures and demonstrated significant variations in EB with modified vdW gap induced by laser irradiation,<sup>[15]</sup> suggesting that the thermal-cycling-assisted modifications to the vdW gap could potentially contribute to the observed evolution of EB.

By examining  $H_{\text{EB}}$  obtained during 15 consecutive cycles for device 1 (Figure 3a,b), we can see that the value of  $H_{\text{EB}}$  varies between a minimum of 25 ( $\pm 5$ ) mT and a maximum of 132 ( $\pm 5$ ) mT which corresponds to an enhancement of > 500% in magnitude. Although device D1 shows a larger mean magnitude of  $H_{\text{EB}}$  (95 mT) in 15 measurements compared to D2 (61 mT) and D3 (68 mT) (refer to Figure S6 in the Supporting Information), the variation of the magnitude of  $H_{\text{EB}}$  is larger ( $\approx 1000\%$ ) in D2 and D3 (refer to Figure S5 in the Supporting Information). Such a huge enhancement in  $H_{\text{EB}}$  by merely thermal cycling is unprecedented and calls for further understanding of the underlying mechanism. For that, we construct a heterostructure with a h-BN-capped MnPS<sub>3</sub>/Fe<sub>3</sub>GeTe<sub>2</sub> configuration on a Si/SiO<sub>2</sub> (300 nm) substrate, and we perform cross-sectional STEM measurements during two consecutive cooling–heating cycles. The findings are presented in Figure 3c–g. The low-resolution high-angle annular dark-field STEM (HAADF-STEM) image of the h-BN/MnPS<sub>3</sub>/Fe<sub>3</sub>GeTe<sub>2</sub> cross-section is provided in Figure 3c. High-resolution STEM imaging of the vdW MnPS<sub>3</sub>/Fe<sub>3</sub>GeTe<sub>2</sub> heterostructure interface is conducted at room temperature. Refer to Figure S7 (Supporting Information) for a summary of STEM sample fabrication and measurements conducted. The scans are repeated at multiple regions to account for any spatial nonuniformity at the interface. A low-resolution STEM image with a larger field of view can be seen in Figure S8 (Supporting Information). By taking the mean of  $\xi$  obtained at different regions, we obtain a value of  $\xi_0 \approx 12$  ( $\pm 3$ ) nm (see Figure 3e) which we define as the intercrystalline distance of MnPS<sub>3</sub> and Fe<sub>3</sub>GeTe<sub>2</sub>. It is evident from the HR-STEM image that  $\xi$  is constituted of the vdW gap and an amorphous region formed by intermigration of atoms between MnPS<sub>3</sub> and Fe<sub>3</sub>GeTe<sub>2</sub> as evident from the STEM–energy dispersive X-ray (EDX) elemental mapping (refer to Figure S9 in the Supporting Information). Subsequently, we reevaluate the interface twice at room temperature, each time on a freshly prepared lamella from the same stack following the ex-situ cooling of the heterostructure to liquid nitrogen (LN<sub>2</sub>) temperature and subsequent warming to room temperature (for experimental details, please refer to the respective Experimental Section). Remarkably,  $\xi$  undergoes significant modification, as evident from the corresponding cross-sectional STEM images (see Figure 3f,g). The values obtained for  $\xi$  after two thermal cycles are  $\xi_1 \approx 7$  ( $\pm 1$ ) and  $\xi_2 \approx 3$  ( $\pm 0.03$ ) nm, respectively, and are summarized in the bar graph (Figure 3d). We observe a reduction of  $\approx 9$  ( $\pm 3$ ) nm in  $\xi$  after two consecutive thermal cycles, which would be in line with the observed change in the magnitude of  $H_{\text{EB}}$  found in all of the three devices. However, we want to emphasize that this complex evolving nature may well be additionally

linked to the magnetic properties of the amorphous layers, which play a significant role in the changing intercrystalline distance, as evidenced by STEM measurements. Additionally, we find that the largest exchange bias is observed after the initial cooling of a freshly prepared device. While this might be related to  $\xi$ , one would need to carry out concurrent imaging and exchange bias measurements, which is beyond the scope of this work.

We further theoretically examined the influence of the vdW gap on the total energy of the MnPS<sub>3</sub>/Fe<sub>3</sub>GeTe<sub>2</sub> heterostructure using first-principle calculations (refer to Figure S10 in the Supporting Information). Our results indicate a strict lower bound on the minimal vdW gap of 6 Å. Furthermore, we observed that the total energy variation for distances exceeding this limit is negligible. This suggests that the system remains stable for finite vdW gaps beyond the defined lower bound and can transition into metastable states with varying vdW gaps at minimal energy expense. The origin of such a significant variation in the intercrystalline distance and the modified vdW gap can be attributed to the thermal-expansion-coefficient-mismatch-induced strain between Fe<sub>3</sub>GeTe<sub>2</sub> and MnPS<sub>3</sub>, which would be significant at the interface.<sup>[30]</sup> Despite the inherent limitations in the controllability of vdW gap alteration using this method, it is a straightforward and efficient approach that can be expanded to tune also other spintronic phenomena related to interfaces<sup>[31,32]</sup> within vdW heterostructures. However, our present capabilities limit the quantification of the structure and magnetic properties of the formed amorphous layers and provide a quantitative description of how they contribute to the evolution of exchange bias. Although several potential factors could contribute, such as strain-induced crystallization, amorphization, or chemical effects at the interface due to varying gap spacings, our current explanation has to remain phenomenological. However, we would like to stress that the amorphization and recrystallization induced by thermal cycling in vdW heterostructure interfaces hold significant importance on its own. We recognize the need to address this issue using more sophisticated and sensitive techniques, which we plan to pursue in a subsequent study that goes beyond the scope of the current work.

### 3. Conclusion

In conclusion, we observed a huge EB in MnPS<sub>3</sub>/Fe<sub>3</sub>GeTe<sub>2</sub> vdW heterostructures despite MnPS<sub>3</sub> having a compensated collinear antiferromagnetic spin structure below the Néel temperature of 78 K. Notably, our experiments reveal that significant exchange bias appears only below 40 K, a phenomenon attributed to an inherent anomalous weak ferromagnetic moment emerging in MnPS<sub>3</sub>. This phenomenon has remained largely unexplored thus far, and it originates from a spin-reorientation transition from an OOP Heisenberg-type order to an IP XY-type order. The magnitude of EB is found to exhibit an evolving nature that leads to a variation of  $H_{\text{EB}}$  up to 1000% achievable merely by thermal cycling. This evolving nature of EB observed is due to the modified interfacial registry of the vdW AFM/FM heterostructure characterized by a modified distance between the crystalline layers and the formation of an amorphous region, as shown by cross-sectional STEM measurements. High-resolution STEM measurements, combined with elemental analysis, reveal the migration of atoms across the vdW gap leading to the formation

of an amorphous region on both FM and AFM layers at the interface. From the observed changes in the interface structure, it is clear that the magnetic coupling will have a complex dependence on the interface, emphasizing the need for thorough interface characterization, for instance, by high-resolution imaging before drawing conclusions on the coupling at interfaces of magnetic van der Waals heterostructures. Our work thus challenges a widely spread belief that van der Waals materials form clean, well-defined, and defect-free interfaces in heterostructures. In particular, one has to note that chemical reactions at the interface do take place even if the materials are individually exhibiting well-defined surfaces. The observed remarkable EB in vdW AFM/FM heterostructures, subject to tunability through straightforward thermal-cycling-induced vdW gap engineering reveals significant potential for the facile manipulation of EB in vdW heterostructures for magnetic storage and sensor applications. This simple strategy can be implemented for tuning other phenomena at interfaces within vdW heterostructures.

#### 4. Experimental Section

**MnPS<sub>3</sub>/Fe<sub>3</sub>GeTe<sub>2</sub> vdW Heterostructure Fabrication:** Bulk “single crystals” of MnPS<sub>3</sub> and Fe<sub>3</sub>GeTe<sub>2</sub> were obtained from the collaborators in the Johannes Kepler University Linz and the Max Planck Institute for Solid State Research Stuttgart, respectively. The bulk crystals were subjected to Raman spectroscopy measurements, and the obtained spectra agreed well with the standard Raman modes expected for MnPS<sub>3</sub><sup>[33]</sup> and Fe<sub>3</sub>GeTe<sub>2</sub><sup>[34]</sup> (refer to Figure S11 in the Supporting Information). The bulk crystals were exfoliated down to a few-layered flakes onto a Si/SiO<sub>2</sub> (300 nm) substrate inside a glove box, with the O<sub>2</sub> and H<sub>2</sub>O levels maintained well below 0.5 ppm. Suitable few-layered flakes of both Fe<sub>3</sub>GeTe<sub>2</sub> and MnPS<sub>3</sub> were selected using an optical microscope. A PDMS- and PMMA-assisted dry transfer method was employed inside the glove box to transfer and stack multilayered flakes of Fe<sub>3</sub>GeTe<sub>2</sub> and MnPS<sub>3</sub> in the specified order. This resulted in the formation of a MnPS<sub>3</sub>/Fe<sub>3</sub>GeTe<sub>2</sub> vdW heterostructure with a clean interface. To minimize the risk of oxidation due to brief exposure of the heterostructure to air during wire bonding of the voltage and current pads for anomalous Hall measurements, the obtained heterostructure was capped with a h-BN flake. Additionally, special care was taken to limit the air exposure time to below 30 min in all the devices measured before loading onto the high field cryostat sample space, where a low-pressure helium environment was maintained during this investigation unless otherwise stated. Atomic force microscopy was carried out to measure the thickness of MnPS<sub>3</sub> and Fe<sub>3</sub>GeTe<sub>2</sub> flakes of the heterostructures (refer to Figure S12 in the Supporting Information).

**Magnetotransport Measurements:** The h-BN-capped MnPS<sub>3</sub>/Fe<sub>3</sub>GeTe<sub>2</sub> heterostructures were then wire-bonded and immediately loaded onto a variable temperature insert cryostat in which a magnetic field up to 12 T could be applied for anomalous Hall effect (AHE) measurements. Since MnPS<sub>3</sub> is an insulating antiferromagnet, the current would only flow through the metallic Fe<sub>3</sub>GeTe<sub>2</sub> layer. The cross-sectional area of the current channel along an 80 nm × 5 μm Fe<sub>3</sub>GeTe<sub>2</sub> flake (device 1) was 4 × 10<sup>-13</sup> m<sup>2</sup>, and was used to calculate the current density, which was ≈ 2.5 × 10<sup>6</sup> A m<sup>-2</sup> for an applied current of 1 μA. A 1 μA current was transmitted through the Fe<sub>3</sub>GeTe<sub>2</sub> flake along the x-direction and the anomalous Hall voltage (V<sub>xy</sub>) was measured across the transverse terminals along the y-direction. The field was always applied in the OOP orientation for the field-cooling process and the field sweeping. A Keithley 2400 source meter was used to flow current through the device, and a Keithley 2182a nanovoltmeter was used to measure voltage.

**DC SQUID Magnetometry Measurements:** Magnetic hysteresis loops (M vs H) and temperature-dependent magnetization curves (M vs T) were acquired for a bulk MnPS<sub>3</sub> crystal using a Quantum Design SQUID MPMS3 magnetometer. The M versus H measurements involved sweep-

ing the magnetic field in both IP and OOP orientations relative to the crystal's bulk structure. Meanwhile, M versus T measurements were conducted over a temperature range of 5–100 K, applying a magnetic field of 50 Oe in an OOP orientation.

**S-NVM Measurements:** S-NVM was a potent, noninvasive imaging technique suitable for probing weak magnetic fields on the order of microtesla with a spatial resolution of 30–100 nm, especially suitable for the investigation of magnetism in vdW nanomagnets.<sup>[35–37]</sup> An all-diamond atomic force tip containing a single NV near the apex of the tip (≈ 10–20 nm) was brought close to the sample's surface.<sup>[38]</sup> The NV center hosted an optically addressable spin that was initialized and read out all optically while it was coherently manipulated by externally applied microwaves. The upper spin levels showed a Zeeman effect, which allowed for a precise measurement of the stray magnetic field along the NV quantization axis.<sup>[39]</sup> S-NVM measurements were performed in a commercial cryogenic atomic force microscopy system (AttoCube, AttoLiquid 1000) with a home-built NV magnetometry setup (details in ref. [40]). For AFM operation, the NV tip was mounted on a quartz capillary glued to a quartz tuning fork. The tuning fork was operated in shear mode with amplitude feedback to keep the tip at a constant height above the surface. The tip was positioned by piezo positioners and scanners, providing a scan range of 15 μm × 15 μm. The complete atomic force microscopy setup was placed in a sample chamber at 100 mbar He atmosphere located in the liquid bath cryostat at a base temperature of 4.3 K. A 0.5 T vector magnet was used to apply an external magnetic field. The emission of a 532 nm laser (Laser Quantum GEM) was collimated on a 0.81 numerical aperture (NA) objective (AttoCube LT-APO) and subsequently focused on the NV. The resulting photoluminescence (PL) was collected via the excitation path and separated by a dichroic mirror (Thorlabs DMLP567). The PL photons were collected by an avalanche photodiode (Excelitas SPCM-AQRH-33). The microwave signal for coherent manipulation of the NV spin was produced by a signal generator (SRS SG384) and an IQ modulator (Polyphase Microwave AM0350A), amplified (Minicircuit ZHL-42W+), and transmitted by a bond wire ≈ 100 nm close to the NV tip. An arbitrary waveform generator (Spectrum instrumentation DN2.663-4) was used to pulse the microwave driving and the laser emission. The resonance frequency of the spin transition was recorded at each pixel to determine the corresponding stray magnetic field from the Zeeman-induced frequency shift. The NV was excited with a 500 μs laser pulse, which initialized the NV into the m<sub>s</sub> = 0 spin state. Next, a near-resonant microwave π pulse was applied to the NV center. The resulting spin state was read out by a second 500 μs laser pulse that also reinitialized the spin state for the following pulse cycle. Two different measurement schemes were used: a) full optical detected magnetic resonance spectra were recorded at each pixel, and b) a feedback protocol was used to track the resonance frequency of the NV. While the first scheme required more integration time but was less prone to measurement artifacts, the second scheme provided higher field sensitivity, resulting in a lower noise level. S-NVM was carried out at a base temperature of 4.5 K, with an external bias field of 150 mT applied along the determined NV axis before the measurements. The NV axis of the tip used for this work was measured to be 56° (± 2°) with the OOP direction. This preapplication of an external bias field aimed to optimize sensor performance at low temperatures.<sup>[41]</sup>

**STEM Measurements:** The STEM imaging was done using a double-corrected TFS Spectra 300 microscope operated in STEM mode at 300 kV. The microscope was equipped with a high-brightness X-FEG, monochromated source, and a piezo CompuStage, and could achieve sub-Ångström resolution. The transmission electron microscopy (TEM) lamella was tilted, so the Fe<sub>3</sub>GeTe<sub>2</sub> was in the <0001> zone axis. A HAADF detector was used to image the interface between the Fe<sub>3</sub>GeTe<sub>2</sub> and MnPS<sub>3</sub>. The intercrystalline distance between the Fe<sub>3</sub>GeTe<sub>2</sub> and MnPS<sub>3</sub> stacks responsible for the exchange coupling was measured using high-resolution STEM. The required TEM lamella was prepared using the focused ion beam (FIB) technique. The lamella was prepared by cutting a stack of Fe<sub>3</sub>GeTe<sub>2</sub>/MnPS<sub>3</sub> on a (300 nm) SiO<sub>2</sub>/Si wafer and encapsulated in h-BN using an FEI make Helios 460F dual beam FIB-SEM. A 5 nm thick Pd layer was deposited on top of the stack to prevent charging. Two protective layers of electron-beam-deposited Pt and ion beam carbon were

deposited atop the area of interest to reduce the sample contamination due to gallium implantation. A TEM lamella with an electron transparent window of  $\approx 50$  nm thickness was cut from the chip, and the distance between the  $\text{Fe}_3\text{GeTe}_2$  and  $\text{MnPS}_3$  layers was measured (see Figure S7 in the Supporting Information for a summary of stepwise STEM cross-section lamella fabrication). To study the change in the intercrystalline distance with cooling cycles, it was preferred to cool down the entire crystal rather than the TEM lamella since the process of lamella fabrication reduced the sample conditions due to the strains introduced due to the production of thin TEM lamella and Ga implantation. The  $\text{SiO}_2/\text{Si}$  chip consisting of the vdW heterostructure was cooled down to 77 K by dropping the chip into  $\text{LN}_2$  in a dewar and waiting at least 8 h until all the  $\text{LN}_2$  evaporated. After the chip warmed up to room temperature, it was dried using a  $\text{N}_2$  gun to remove any moisture condensing on the surface. Additional TEM lamellae were prepared after each cooling cycle to measure the intercrystalline distance. EDX spectroscopy was carried out using an FEI Titan TEM equipped with a Schottky field emission gun operated at 200 kV, a CEOS probe aberration corrector, a HAADF, and a Super-X EDX detection system. Elemental maps and profiles were obtained using the Thermo Scientific Velox software. The results are summarized in Figure S9 (Supporting Information).

**First-Principle Calculations:** First-principle calculations were performed using the VASP software package.<sup>[42–45]</sup> Distances between 5 and 12 Å were chosen and a full spin-polarized self-consistency with FM and AFM starting ground states were chosen for FGT and MNPS<sub>3</sub>, respectively. The calculations were performed using the GGA exchange correlation functional<sup>[46]</sup> and converged on an 8 by 8 *k*-mesh with an energy cutoff of 270 eV. The results are summarized in Figure S10 (Supporting Information).

## Supporting Information

Supporting Information is available from the Wiley Online Library or from the author.

## Acknowledgements

A.P.B. and A.K. contributed equally to this work. The authors acknowledge funding from the Alexander von Humboldt Foundation for Humboldt Postdoctoral Fellowship (Grant Number: Ref 3.5-IND-1216986-HFST-P), the EU Marie-Curie Postdoctoral Fellowship ExBiaVdW (Grant Number: 101068014), the Deutsche Forschungsgemeinschaft (DFG, German Research Foundation) – Spin + X TRR 173–268565370 (Projects Nos. A01, B02, and A12), DFG Project No. 358671374, the Graduate School of Excellence Materials Science in Mainz (MAINZ) GSC 266, the MaHoJeRo (DAAD Spintronics network, Projects Nos. 57334897 and 57524834), the Research Council of Norway (Center for Quantum Spintronics – QuSpin No. 262633), The European Union’s Horizon 2020 Research and Innovation Programme under Grant agreement No. 856538 (project “3D MAGIC”). S.F. acknowledges the China Scholarship Council for financial support. Additionally, the authors wish to express their gratitude to Dr. Arnab Bose for the insightful discussions.

Open access funding enabled and organized by Projekt DEAL.

## Data Availability Statement

The data that support the findings of this study are available from the corresponding author upon reasonable request.

## Keywords

exchange bias,  $\text{Fe}_3\text{GeTe}_2$ , manganese thiophosphate, vdW heterostructures, vdW magnetic materials

Received: March 12, 2024  
Revised: June 24, 2024  
Published online: July 12, 2024

- [1] T. Blachowicz, A. Ehrmann, M. Wortmann, *Nanomaterials*. **2023**, *13*, 2418.
- [2] W. H. Meiklejohn, C. P. Bean, *Phys. Rev.* **1957**, *105*, 904.
- [3] T. Blachowicz, A. Ehrmann, *Coatings*. **2021**, *11*, 122.
- [4] K. O’Grady, L. E. Fernandez-Outon, G. Vallejo-Fernandez, *J. Magn. Magn. Mater.* **2010**, *322*, 883.
- [5] L. Néel, *Ann. Phys.* **1967**, *14*, 61.
- [6] D. Mauri, H. C. Siegmann, P. S. Bagus, E. Kay, *J. Appl. Phys.* **1987**, *62*, 3047.
- [7] R. Yanes, J. Jackson, L. Udvardi, L. Szunyogh, U. Nowak, *Phys. Rev. Lett.* **2013**, *111*, 217202.
- [8] A. P. Malozemoff, *Phys. Rev. B*. **1987**, *35*, 3679.
- [9] T. C. Schulthess, W. H. Butler, *Phys. Rev. Lett.* **1998**, *81*, 4516.
- [10] P. Miltényi, M. Gierlings, J. Keller, B. Beschoten, G. Güntherodt, U. Nowak, K. D. Usadel, *Phys. Rev. Lett.* **2000**, *84*, 4224.
- [11] M. Gibertini, M. Koperski, A. F. Morpurgo, K. S. Novoselov, *Nat. Nanotechnol.* **2019**, *14*, 408.
- [12] M.-H. Phan, V. Kalappattil, V. O. Jimenez, Y. Thi Hai Pham, N. W. Y. A. Y. Mudiyansele, D. Detellem, C.-M. Hung, A. Chanda, T. Eggers, *J. Alloys Compd.* **2023**, *937*, 168375.
- [13] C. Hu, K. N. Gordon, P. Liu, J. Liu, X. Zhou, P. Hao, D. Narayan, E. Emmanouilidou, H. Sun, Y. Liu, H. Brawer, A. P. Ramirez, L. Ding, H. Cao, Q. Liu, D. Dessau, N. Ni, *Nat. Commun.* **2020**, *11*, 97.
- [14] T. Li, S. Jiang, N. Sivasdas, Z. Wang, Y. Xu, D. Weber, J. E. Goldberger, K. Watanabe, T. Taniguchi, C. J. Fennie, K. Fai Mak, J. Shan, *Nat. Mater.* **2019**, *18*, 1303.
- [15] X. Huang, L. Zhang, L. Tong, Z. Li, Z. Peng, R. Lin, W. Shi, K.-H. Xue, H. Dai, H. Cheng, D. de Camargo Branco, J. Xu, J. Han, G. J. Cheng, X. Miao, L. Ye, *Nat. Commun.* **2023**, *14*, 2190.
- [16] Z. Ying, B. Chen, C. Li, B. Wei, Z. Dai, F. Guo, D. Pan, H. Zhang, D. Wu, X. Wang, S. Zhang, F. Fei, F. Song, *Nano Lett.* **2023**, *23*, 765.
- [17] S. Albarakati, W.-Q. Xie, C. Tan, G. Zheng, M. Algarni, J. Li, J. Partridge, M. J. S. Spencer, L. Farrar, Y. Xiong, M. Tian, X. Wang, Y.-J. Zhao, L. Wang, *Nano Lett.* **2022**, *22*, 6166.
- [18] T. Zhang, Y. Zhang, M. Huang, B. Li, Y. Sun, Z. Qu, X. Duan, C. Jiang, S. Yang, *Adv. Sci.* **2022**, *9*, 2105483.
- [19] A. Puthirath Balan, A. Kumar, T. Scholz, Z. Lin, A. Shahee, S. Fu, T. Denneulin, J. Vas, A. Kovács, R. E. Dunin-Borkowski, H. I. Wang, J. Yang, B. V. Lotsch, U. Nowak, M. Kläui, *ACS Nano*. **2024**, *18*, 8383.
- [20] C. Tan, J. Lee, S.-G. Jung, T. Park, S. Albarakati, J. Partridge, M. R. Field, D. G. McCulloch, L. Wang, C. Lee, *Nat. Commun.* **2018**, *9*, 1554.
- [21] P. A. Joy, S. Vasudevan, *Phys. Rev. B*. **1992**, *46*, 5425.
- [22] G. Long, H. Henck, M. Gibertini, D. Dumcenco, Z. Wang, T. Taniguchi, K. Watanabe, E. Giannini, A. F. Morpurgo, *Nano Lett.* **2020**, *20*, 2452.
- [23] R. Zhu, W. Zhang, W. Shen, P. K. J. Wong, Q. Wang, Q. Liang, Z. Tian, Y. Zhai, C.-w. Qiu, A. T. S. Wee, *Nano Lett.* **2020**, *20*, 5030.
- [24] A. R. Wildes, S. J. Kennedy, T. J. Hicks, *J. Phys.: Condens. Matter* **1994**, *6*, L335.
- [25] E. Ressouche, M. Loire, V. Simonet, R. Ballou, A. Stunault, A. Wildes, *Phys. Rev. B*. **2010**, *82*, 100408.
- [26] K. Kurosawa, S. Saito, Y. Yamaguchi, *J. Phys. Soc. Jpn.* **1983**, *52*, 3919.
- [27] S. Chaudhuri, C. N. Kuo, Y. S. Chen, C. S. Lue, J. G. Lin, *Phys. Rev. B*. **2022**, *106*, 094416.
- [28] H. Han, H. Lin, W. Gan, R. Xiao, Y. Liu, J. Ye, L. Che, W. Wang, L. Zhang, C. Zhang, H. Li, *Phys. Rev. B*. **2023**, *107*, 075423.
- [29] J. Dubowik, I. Gościńska, *Acta Phys. Pol.*, **A**. **2015**, *127*, 147.

- [30] L. Zhang, H. Wang, X. Zong, Y. Zhou, T. Wang, L. Wang, X. Chen, *Nat. Commun.* **2022**, *13*, 3996.
- [31] F. Hellman, A. Hoffmann, Y. Tserkovnyak, G. S. D. Beach, E. E. Fullerton, C. Leighton, A. H. MacDonald, D. C. Ralph, D. A. Arena, H. A. Dürr, P. Fischer, J. Grollier, J. P. Heremans, T. Jungwirth, A. V. Kimel, B. Koopmans, I. N. Krivorotov, S. J. May, A. K. Petford-Long, J. M. Rondinelli, N. Samarth, I. K. Schuller, A. N. Slavin, M. D. Stiles, O. Tchernyshyov, A. Thiaville, B. L. Zink, *Rev. Mod. Phys.* **2017**, *89*, 025006.
- [32] P. Kumar, J. Liu, M. Motlag, L. Tong, Y. Hu, X. Huang, A. Bandopadhyay, S. K. Pati, L. Ye, J. Irudayaraj, G. J. Cheng, *Nano Lett.* **2018**, *19*, 283.
- [33] Y.-J. Sun, Q.-H. Tan, X.-L. Liu, Y.-F. Gao, J. Zhang, *J. Phys. Chem. Lett.* **2019**, *10*, 3087.
- [34] X. Kong, T. Berlijn, L. Liang, *Adv. Electron. Mater.* **2021**, *7*, 2001159.
- [35] L. Thiel, Z. Wang, M. A. Tschudin, D. Rohner, I. Gutiérrez-Lezama, N. Ubrig, M. Gibertini, E. Giannini, A. F. Morpurgo, P. Maletinsky, *Science* **2019**, *364*, 973.
- [36] T. Song, Q.-C. Sun, E. Anderson, C. Wang, J. Qian, T. Taniguchi, K. Watanabe, M. A. McGuire, R. Stöhr, D. Xiao, T. Cao, J. Wrachtrup, X. Xu, *Science* **2021**, *374*, 1140.
- [37] A. Laraoui, K. Ambal, *Appl. Phys. Lett.* **2022**, *121*, 060502.
- [38] P. Appel, E. Neu, M. Ganzhorn, A. Barfuss, M. Batzer, M. Gratz, A. Tschöpe, P. Maletinsky, *Rev. Sci. Instrum.* **2016**, *87*, 063703.
- [39] L. Rondin, J. P. Tetienne, T. Hingant, J. F. Roch, P. Maletinsky, V. Jacques, *Rep. Prog. Phys.* **2014**, *77*, 056503.
- [40] L. Thiel, D. Rohner, M. Ganzhorn, P. Appel, E. Neu, B. Müller, R. Kleiner, D. Koelle, P. Maletinsky, *Nat. Nanotechnol.* **2016**, *11*, 677.
- [41] J. Happacher, D. A. Broadway, J. Bocquel, P. Reiser, A. Jimenez, M. A. Tschudin, L. Thiel, D. Rohner, M. I. G. Puigibert, B. Shields, J. R. Maze, V. Jacques, P. Maletinsky, *Phys. Rev. Lett.* **2022**, *128*, 177401.
- [42] G. Kresse, J. Hafner, *Phys. Rev. B.* **1993**, *47*, 558.
- [43] G. Kresse, J. Hafner, *Phys. Rev. B.* **1994**, *49*, 14251.
- [44] G. Kresse, J. Furthmüller, *Comput. Mater. Sci.* **1996**, *6*, 15.
- [45] G. Kresse, J. Furthmüller, *Phys. Rev. B.* **1996**, *54*, 11169.
- [46] J. P. Perdew, K. Burke, M. Ernzerhof, *Phys. Rev. Lett.* **1996**, *77*, 3865.
- [47] J.-Z. Fang, H.-N. Cui, S. Wang, J.-D. Lu, G.-Y. Zhu, X.-J. Liu, M.-S. Qin, J.-K. Wang, Z.-N. Wu, Y.-F. Wu, S.-G. Wang, Z.-S. Zhang, Z. Wei, J. Zhang, B.-C. Lin, Z.-M. Liao, D. Yu, *Phys. Rev. B.* **2023**, *107*, L041107.
- [48] H. Dai, H. Cheng, M. Cai, Q. Hao, Y. Xing, H. Chen, X. Chen, X. Wang, J.-B. Han, *ACS Appl. Mater. Interfaces.* **2021**, *13*, 24314.
- [49] T. M. Cham, R. J. Dorria, X. S. Zhang, A. H. Dismukes, D. G. Chica, A. F. May, X. Roy, D. A. Muller, D. C. Ralph, Y. K. Luo, *Adv. Mater.* **2024**, *36*, 2305739.